Tenth International Conference on Computational Fluid Dynamics (ICCFD10), Barcelona,Spain, July 9-13, 2018

ICCFD10-2018-xxxx

On the boundary layer development and heat transfer from a sphere at moderate Reynolds numbers

I. Rodriguez*, O. Lehmkuhl**, M. Soria*, S. Gómez**,
M. Domínguez-Pumar*** and L. Kowalski***
Corresponding author: ivette.rodriguez@upc.edu

* Turbulence and Aerodynamics Research Group (TUAREG). Universitat Politècnica de Catalunya-BarcelonaTech. Spain
** Barcelona Supercomputing Centre (BSC)
*** Departamento de Ingeniería Electrónica (DEE). Grupo Micro y NanoTecnología (MNT). Universitat Politècnica de Catalunya-BarcelonaTech

Abstract: Direct and large-eddy numerical simulations have been performed for a heated sphere at Reynolds numbers 200, 300, 500, 750, 1000 and 10^4, in the context of the development of a spherical wind sensor for Mars atmosphere intended for missions after Rover 2020. A low-dissipation finite element scheme implemented in the multi-physics code Alya has been used to do so. The main heat transfer and aerodynamic parameters are presented, followed by detailed analysis of the wake and boundary layer development and the local heat transfer coefficients. Viscous and thermal boundary layer thicknesses decrease with the Reynolds number, the thermal one being thicker than the viscous layer. However, in all cases shape factor is the same in the zone with the favourable pressure gradient. The local Nusselt number is found to be asymmetric in the rear zone of the sphere for the laminar cases and recover its statistical symmetry once the wake transition to turbulent flow. It is also found that the stagnation Nusselt number scales as $Re^{0.47}$, in fair agreement with previous studies.

Keywords: wakes, DNS, LES, viscous and thermal boundary layer

1 Introduction

The knowledge about fluid dynamics and heat transfer from spherical bluff bodies is of key importance in many engineering applications and science such as dispersed particle-laden, sprays, etc. For Reynolds numbers larger than 300 ($Re = 300$), the flow is dominated by the shedding of vortices with a laminar wake up to $Re = 800$ [1]. For larger Reynolds numbers, a Kelvin-Helmholtz instability is responsible for the inception of small-scales structures in the separated shear layer and the transition to turbulence in the wake. However, although the wake becomes turbulent, the attached boundary layer remains laminar up until $Re < 3 \times 10^5$; this regime is also known as subcritical regime. The turbulent wake and the unsteady shedding of vortices from a sphere have been subject of many experimental investigations (see for instance [1, 2, 3, 4]) and in less extent by numerical simulations (e.g. [5, 6, 7] and citations therein). Moreover, at low-to-moderate Reynolds numbers the flow characteristics are dominated by a low-frequency mechanism that alters the way vortex are shed and thus, the wake dynamics [5].

Regarding the heat transfer, measurements of the local and overall Nusselt number have been extensively reported in the literature (e.g. [8, 9, 10]). However few studies can be found about the boundary layer development and its role on the wake dynamics from heated spheres.

The present work is motivated for the development of a spherical wind sensor for Mars atmosphere[11], intended for future missions after Rover 2020. Thus, the analysis of the thermal interaction of the sphere with the wind for Mars atmosphere is a key aspect of its design, although other applications for the Earth atmosphere have also been considered.

In this sense, the present works aims at analysing the boundary layer development and heat transfer from a sphere at the moderate Reynolds numbers in the range of $Re = 300 - 10^4$ and $Pr = 0.7$. The lower Reynolds numbers are related to conditions in Mars, including extreme conditions such as dust devils, whereas the larger Reynolds number are for Earth atmosphere applications.

2 Mathematical and numerical models

The incompressible Navier-Stokes and energy equations can be written as

$$\frac{\partial u_i}{\partial x_i} = 0 \tag{1}$$

$$\frac{\partial u_i}{\partial t} + \frac{\partial u_i u_j}{\partial x_j} - \nu \frac{\partial^2 u_i}{\partial x_j \partial x_j} + \rho^{-1} \frac{\partial p}{\partial x_i} = 0 \tag{2}$$

$$\frac{\partial T}{\partial t} + \frac{\partial u_i T}{\partial x_j} - \kappa \frac{\partial^2 T_i}{\partial x_j \partial x_j} = 0 \tag{3}$$

where x_i are the spatial coordinates (or x, y, and z), u_i (or u, v, and w) stands for the velocity components and p and T are the pressure and temperature fields; ν is the kinematic viscosity, ρ the density of the fluid and κ is its thermal diffusivity.

For the LES, the above equations are spatially filtered, so the filtered equations are,

$$\frac{\partial \overline{u}_i}{\partial x_i} = 0 \tag{4}$$

$$\frac{\partial \overline{u}_i}{\partial t} + \frac{\partial \overline{u}_i \overline{u}_j}{\partial x_j} - \nu \frac{\partial^2 \overline{u}_i}{\partial x_j \partial x_j} + \rho^{-1} \frac{\partial \overline{p}}{\partial x_i} = -\frac{\partial \mathcal{T}_{ij}}{\partial x_j} \tag{5}$$

$$\frac{\partial \overline{T}}{\partial t} + \frac{\partial \overline{u}_i \overline{T}}{\partial x_j} - \kappa \frac{\partial^2 \overline{T}_i}{\partial x_j \partial x_j} = \frac{\partial \mathcal{T}_{Tij}}{\partial x_j} \tag{6}$$

where $(\bar{\cdot})$ stands for the filtered variables. The terms $\mathcal{T}_{ij}$ and $\mathcal{T}_{Tij}$, the sub-grid stresses and subgrid-scale heat fluxes in equations 5 and 6 resulting from the filtering of the non-linear terms must be modelled. The anisotropic part of the subgrid stress tensor (SGS) is given as,

$$\mathcal{T}_{ij} - \frac{1}{3}\mathcal{T}_{kk}\delta_{ij} = -2\nu_{sgs}\overline{\mathcal{S}}_{ij} \tag{7}$$

where $\overline{\mathcal{S}}_{ij} = \frac{1}{2}(g_{ij} + g_{ji})$ is the large-scale rate-of-strain tensor, and $g_{ij} = \partial \overline{u}_i / \partial x_j$; δ_{ij} is the Kronecker delta. The formulation is closed by an appropriate expression for the subgrid-scale viscosity, ν_{sgs}. In this work, the model proposed by Vreman [12] is used. $\mathcal{T}_{Tij}$ is modelled in a similar manner as $\mathcal{T}_{ij}$ but in the expression ν_{sgs} is substituted by $\kappa_{sgs} = \nu_{sgs}/Pr_t$, being Pr_t the turbulent Prandtl number. Here, it is assumed $Pr_t = 0.7$.

The above equations are solved by means of a low-dissipation finite element (FE) scheme [13]. The basic idea behind this approach is to mimic the fundamental symmetry properties of the underlying differential operators, i.e., the convective operator is approximated by a skew-symmetric matrix and the diffusive operator by a symmetric, positive-definite matrix. The chosen low dissipation FE scheme presents good accuracy compared to other low dissipation finite volume and finite difference methods with the advantage of being able to increase the order of accuracy at will without breaking the fundamental symmetry properties of the discrete operators. A non-incremental fractional-step method is used to stabilise the pressure. This allows for the use of finite element pairs that do not satisfy the inf-sup conditions, such as equal order interpolation for the velocity and pressure used in this work. The set of equations is time integrated using an energy conserving Runge-Kutta explicit method lately proposed by Cappuano et al. [14] combined with an eigenvalue

Table 1: Meshes used in the simulation. N_{CVs}, total number of elements, N_{dof} number of degree-of-freedom, Δ_{sph} size of the elements on the surface of the sphere, Δ_{z1} to Δ_{z4} size of the elements in the regions 1 to 4 in the wake of the sphere.

Mesh	N_{CVs}	N_{dof}	Δ_{sph}	Δ_{z1}	Δ_{z2}	Δ_{z3}	Δ_{z4}
m1	9.6×10^6	1.7×10^6	0.0050	0.05	0.08	0.12	0.75
m2	3.27×10^7	5.6×10^6	0.0025	0.025	0.05	0.12	0.75

based time-step estimator [15]. This methodology is implemented into Alya code, which is a multi-physics parallel code organized in a modular way: kernel, services and modules, which can be separately compiled and linked. Each module represents a single set of Partial Differential Equations (PDE) for a given physical model. To solve a coupled multi-physics problem, all the required modules must be active and interacting following a well-defined workflow. For more details, the reader is referred to [16].

2.1 Definition of the cases and boundary conditions

The fluid dynamics and heat transfer around a heated sphere at Reynolds numbers of $Re = 200, 300, 500, 750$, 1000, 10^4 and Prandtl number $Pr = \nu/\kappa = 0.7$ are considered. Here, the Reynolds number $Re = U_{ref}\, D/\nu$ is defined in terms of the free-stream velocity U_{ref} and the sphere diameter D. The thermo-physical properties are set so as to obtain the desired Reynolds and Prandtl numbers. For Reynolds numbers up to $Re = 1000$, direct numerical simulations (DNS) have been performed, whereas for $Re = 10^4$ the flow has been solved by means of large-eddy simulations (LES).

The cases are solved in a cylindrical computational domain of dimensions $x \equiv [-5.5D : 25.5D]$; $r \equiv [0, 10D]$; $\phi \equiv [0, 2\pi]$ with the sphere located at $(0, 0, 0)$. This domain has similar dimensions to that used in the DNS of Rodriguez et al. [5, 6].

The boundary conditions at the inflow consist of a uniform velocity and temperature $(u/U_{ref}, v/U_{ref}, w/U_{ref}) = (1, 0, 0)$. Being the non-dimensional temperature expressed as $\Theta = (T - T_{in})/(T_{sph} - T_{in})$, $\Theta = 0$ has been set at the inlet. T_{sph} and T_{in} are the actual values of the temperature at the sphere surface and at the inlet, respectively, but their values are irrelevant to the problem studied as the velocity and temperature fields are not coupled and the temperature is treated here as a passive scalar. At the outlet, a pressure-based condition has been used (see for instance [5]). At the sphere surface, a non-slip boundary condition has been defined for the velocities and a Dirichlet condition for the temperature $\Theta = 1$ has been prescribed. In the lateral boundary of the domain, tangential velocities and the derivative of the stream-wise component of the velocity are set to zero. For the temperature, Neumann conditions $(\partial T/\partial n = 0)$ are used at the lateral and outflow boundaries.

2.2 Grid sensitiveness study

The computational meshes are designed as follows. Three inner cylindrical regions of radius 1.5D, the outer boundary extends to $x/D = 3.5$, 8.5, 20 from the sphere center are generated. The sizes of the elements at these zones are given in Table 1 and are denoted as Δ_{z1}, Δ_{z2} and Δ_{z3}, respectively. The size of the outer/external zone Δ_{z4} is also given in the table. To generate the mesh, first the superficial mesh with element size of Δ_{sph} (see Table 1) is generated. A view of the central plane of the domain, where the different zones can be seen is shown in figure 1.

The grid sensitivity study has been performed for the two largest Reynolds numbers, which are the more demanding from a computational point of view. The results of the simulations for the two levels of refinement are compared to those of the literature. At $Re = 1000$, with the DNS results by Tomboulides & Orszag [17], where are at $Re = 10^4$, the statistical data have been compared to the DNS results of Rodriguez et al. [6]. All the results presented in the present paper have been integrated in time, once the flow has entered in the statistical stationary regime. For the lower Reynolds numbers (up to $Re = 750$), except for Re=200 where the flow is steady, solutions have been averaged during 150 TU. For the larger Reynolds numbers, i.e. $Re = 1000$ and $Re = 10^4$, the integration time has been for about 300TU and 250TU.

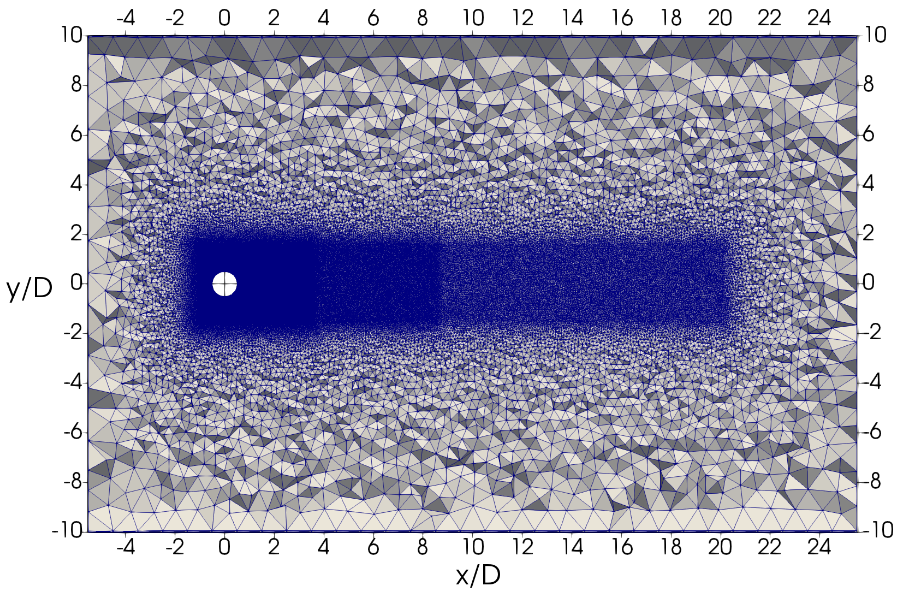

Figure 1: Projection of the central plane of the computation domain. The mesh distribution with the different zones in the domain can be observed. The sphere is located at (0,0,0).

Table 2: Mesh sensitiveness study. Flow parameters for Reynolds numbers $Re = 1000$ and $Re = 1 \times 10^4$ and comparison with literature results. Drag coefficient C_d, fluctuating drag $C_{d,rms}$, fluctuating y-force $C_{y,rms}$, base pressure coefficient $-C_{pb}$, separation angle θ_{sep}, non-dimensional vortex shedding frequency St.

mesh	C_d	$C_{d,rms}$	$C_{y,rms}$	$-C_{pb}$	θ_{sep}	St
$Re = 1000$ (DNS)						
m1	0.466	0.0072	0.0186	0.211	101.1	0.178
m2	0.466	0.0076	0.0210	0.213	101.4	0.200
Sakamoto & Haniu [18]	-	-	-	-	-	0.200
Tomboulides &Orszag (DNS) [17]	-	-	-	-	102.0	0.195
$Re = 10^4$ (LES)						
m1	0.406	0.0093	0.025	0.298	89.9	0.213
m2	0.402	0.0071	0.022	0.293	90.0	0.216
Constantinescu et al.[19] (LES)	0.393	-	-	0.229	85.0	0.195
Yun et al. [20](LES)	0.393	-	-	0.274	90.0	0.170
Rodriguez et al.[6](DNS)	0.402	-	-	0.272	84.7	0.195

Table 3: Heat transfer and aerodynamic coefficients at different Reynolds numbers. Drag coefficient C_d, fluctuating drag $C_{d,rms}$, fluctuating y-force $C_{y,rms}$, separation angle θ_{sep}, non-dimensional vortex shedding frequency St, Nusselt number Nu.

Re	C_d	$C_{d,rms}$	$C_{y,rms}$	θ_{sep}	St	Nu
200	0.773	3.63×10^{-4}	4.58×10^{-5}	117.2	-	9.04
300	0.659	3×10^{-3}	0.011	113.7	0.133	10.63
500	0.562	0.011	0.031	108.5	0.152	13.16
750	0.502	0.009	0.028	104.1	0.175	15.61
1000	0.466	0.0076	0.021	101.5	0.200	17.40
10^4	0.402	0.0071	0.022	90.0	0.216	54.93

The results of some of the flow features obtained are shown in Table 2, where the mean drag coefficient, C_d, and its root mean square $C_{d,rms}$ value, the root mean square value of the y-force coefficient, $C_{y,rms}$, the base pressure coefficient, $-C_{pb}$, the separation angle θ_{sep} measured from the front stagnation point and the non-dimensional vortex shedding-frequency, St are given. As can be seen, even the coarse mesh reproduces quite well the main flow features for both Reynolds numbers. However, as expected, m2 gives slightly better results. In what follows, all the results presented for the larger Reynolds numbers are given with mesh m2, whereas for Reynolds numbers up to $Re = 750$, m1 is used.

3 Results

The main heat transfer and aerodynamic parameters for all Reynolds numbers are given in Table 3. In the table the drag coefficient, the fluctuating lift and drag, the separation angle and non-dimensional vortex shedding frequency are given.As expected, the drag coefficient rapidly decreases with the Reynolds number for the laminar cases. When the wake flow enters in the subcritical regime $Re > 1000$, the drag coefficient stabilizes being almost constant about $C_D = 0.4$ up until turbulent transition occurs in the attached boundary layer and the flow enters the critical regime ($Re \approx 2 \times 10^5$)[2]. In general, there is a good agreement with the experimental results reported in the literature (not shown here). It should be pointed out that at $Re = 200$, the flow is steady and axisymmetric and thus there are not fluctuations of the lift and drag coefficients. Actually, it has been reported in the literature that the onset of vortex shedding is about $Re \approx 210$ [4, 21, 17].

3.1 Wake and boundary layer development

In the range of Reynolds numbers concerning the present paper, significative changes in the wake of the sphere occur. The vortical structures in the range of $Re = 300$ to $Re = 10^4$ are shown in figures 2 and 3. These structures are represented by means of iso-countours of the second-invariant of the velocity gradient tensor Q[22]. According to the Q criterion, a vortical structure is identified in a region with positive Q, i.e. a region where vorticity overcomes strain. To well capture these structures the value of the Q-isosurface represented is increased as the Reynolds number increases. At the lower Reynolds numbers, vortical structures are laminar and thus, correspond with low values of Q. After the onset of the vortex shedding (i.e. at $Re \approx 210$), vortices are shed in an asymmetric manner and then, the wake behind the sphere is also asymmetric as can be seen from the figure 2. Actually, the vertical and lateral forces on the sphere are not equal, being their value larger than zero. This asymmetry is a characteristic thread of the laminar vortex shedding in the sphere and has been reported before both experimentally and numerically (see for instance [2, 21, 17, 23]).

Once the Reynolds number increases beyond $Re = 800$ [1], the shedding of vortices occurs at random locations and thus, the wake recovers its statistic symmetry. At Reynolds number, $Re = 1000$ (see figure 3), the hairpin-like structures detached from the sphere form regular vortex packets that move downstream in a helical-like manner similar to the ones observed at a relatively larger Reynolds number of $Re = 3700$ by Rodriguez et al. [5]. The large scale vortices shed from the sphere break into small-scale structures forming

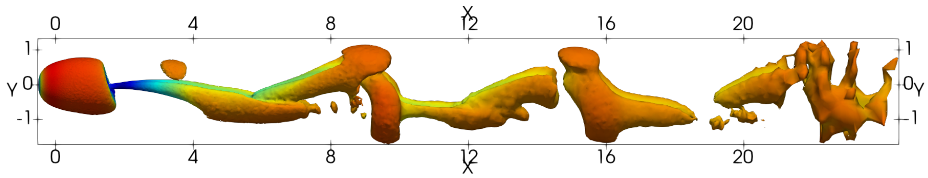

(a)

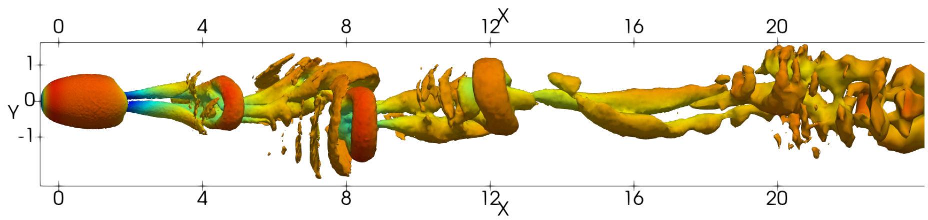

(b)

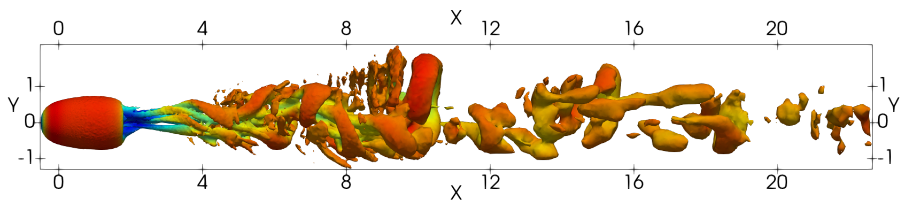

(c)

Figure 2: Laminar vortical structures in the wake of the sphere. (a) $Re = 300$, (b) $Re = 500$, (c) $Re = 750$.

a turbulent wake at $Re = 10^4$. Notice also the Kelvin-Helmholtz like structures in the separated laminar part of the shear layer and how these instabilities trigger the transition to turbulence (figure 3b).

Apart from the differences in the vortical structures shed into the wake, separation from the sphere changes when the Reynolds numbers increase from 200 to 10^4. At $Re \leq 1000$, separation occurs past the apex of the sphere (see location reported in table 2). When the flow stabilizes around $Re = 3000$, the separation point moves backwards towards the apex and it remains in the same location during the whole sub-critical regime up until the drag crisis occurs [1].

The viscous and thermal boundary layer thicknesses and the shape factor for all Reynolds numbers are given in figures 4 and 5. Here, viscous boundary layer thickness (δ_{95}) is defined as the location where the velocity is the 95% of the velocity at the outer edge of the boundary layer. In a similar manner, the thermal boundary layer thickness δ_Θ is defined as the location where the non-dimensional temperature is 5% above the temperature of the free-stream, i.e. $\Theta_{in} = 0$. The shape factor, H, is the ratio of the displacement, δ_1, to the momentum thicknesses, δ_2. Being v_θ the stream-wise velocity in the boundary layer of the sphere, U_e the velocity at the edge of the boundary layer and n the normal direction to the surface of the sphere, these quantities are defined as,

$$\delta_1 = \int_0^{\delta_{95}} \left(1 - \frac{v_\theta}{U_e}\right) dn; \quad \delta_2 = \int_0^{\delta_{95}} \frac{v_\theta}{U_e} \left(1 - \frac{v_\theta}{U_e}\right) dn. \tag{8}$$

As expected, as the Reynolds number increases the boundary layer becomes thinner, and as $Pr < 1$, the

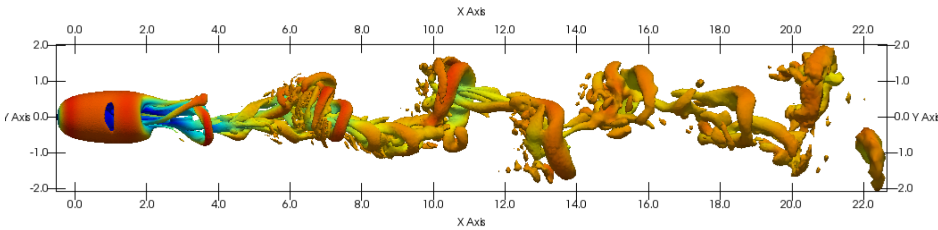

(a)

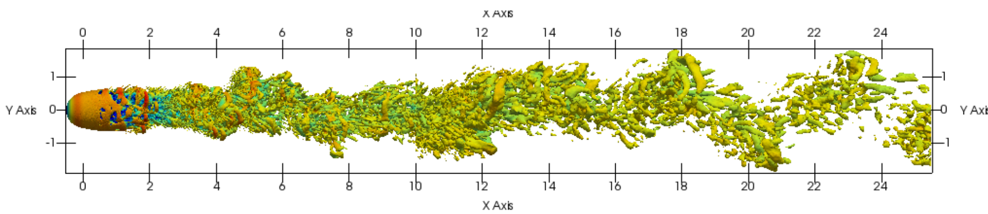

(b)

Figure 3: Vortical structures in the wake of the sphere. (a) $Re = 1000$, (b) $Re = 10^4$.

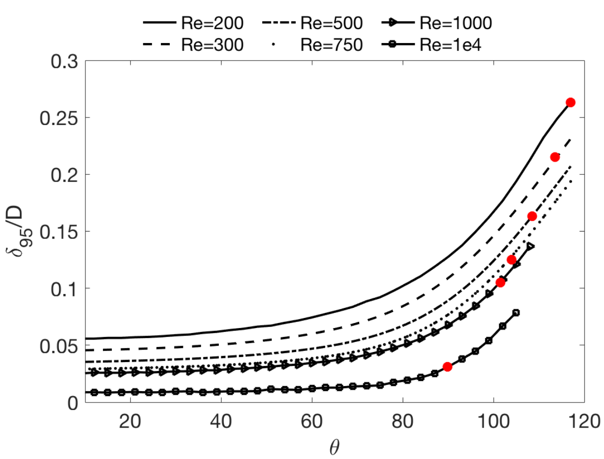

(a)

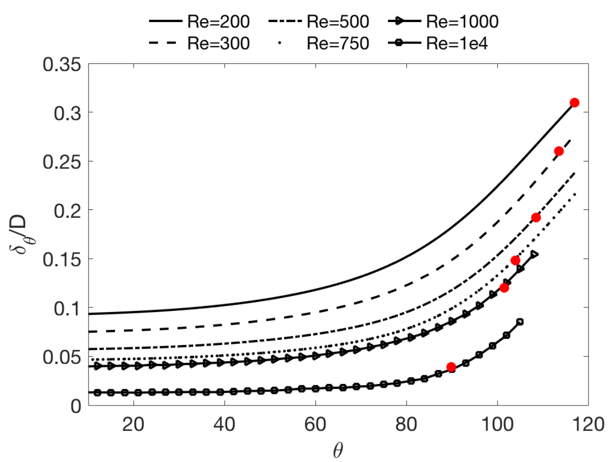

(b)

Figure 4: (a) Viscous and (b) thermal boundary layer thicknesses at the different Reynolds numbers. (red dot) location of the separation point.

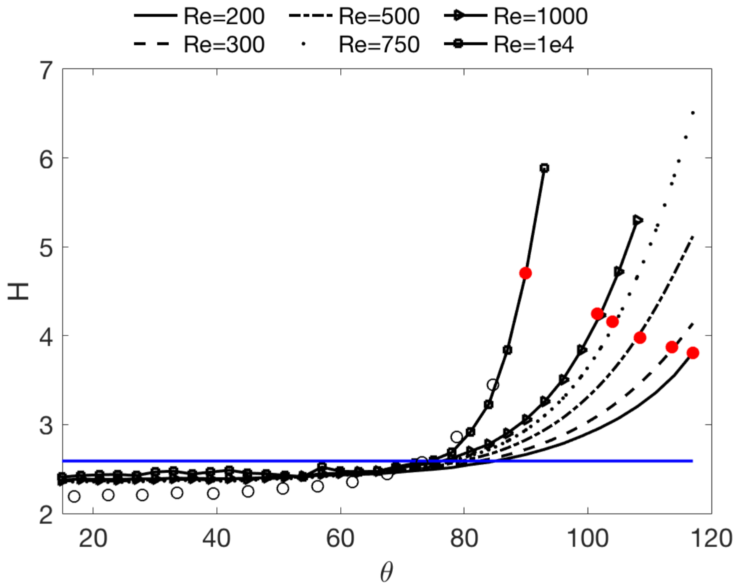

Figure 5: Boundary layer shape factor at the different Reynolds numbers. (red dot) location of the separation point, (blue line) Blausius boundary layer shape factor, (open circles) circular cylinder shape factor.

thermal boundary layer is thicker than the viscous one (see figure 4). Notice that in both figures the location of the separation point is marked as a red dot.

The shape factor shows a more interesting behaviour. For all Reynolds numbers, at low angles from the front stagnation point, the boundary layers have the same shape factor which is slightly lower than the value predicted by Blasius solution for a laminar boundary layer, $H = 2.59$ (blue line in figure 5). Initially, the shape factor shows a slight and constant increase trend up until a certain angle $\theta \approx 70°$. This zone corresponds with the favorable pressure gradient zone, where the flow in the boundary layer accelerates. The viscous and thermal boundary layer thicknesses (see figure 4) keep almost constant with a slight increment in this zone. Once the boundary layer enters the adverse pressure gradient zone and approaches separation, the boundary layer thicknesses and the shape factor rapidly increase. The separation of the boundary layer is eventually reached at $H \approx 3.8 - 4.7$. The location of the separation point is marked in the figure with a solid red dot. The value of the shape factor at separation slightly increases with the Reynolds number. Notice also that the shape factor for the circular cylinder at subcritical Reynolds numbers is also included in the figure for comparison [24]. It is interesting to point out that shape factors for both sphere and cylinder at these Reynolds numbers behave similarly as in both cases the boundary layer is laminar before separation. As the minimum pressure gradient being attained at around $\theta = 70°$, the zone where the boundary layer accelerates and enters the adverse pressure gradient is approximately the same in both cases.

3.2 Heat transfer from the sphere

The Nusselt number at the surface of the sphere is defined as $Nu = h\,D/k$, h being the local dimensional convective heat transfer coefficient and k the thermal conductivity, defined as:

$$h = \frac{k\partial < T > /\partial n}{(T_{sph} - T_{in})D} = k\frac{\partial \Theta}{\partial n} \quad (9)$$

where $< \cdot >$ stands for the average in time fields. Surface average Nusselt numbers are given in Figure 6. Reference values obtained from correlations reported in the literature are also given. In general, the agreement of the average Nusselt number with those reported in the literature is quite good. Yet, among the different references there are also some discrepancies. Actually, there are different issues that can affect

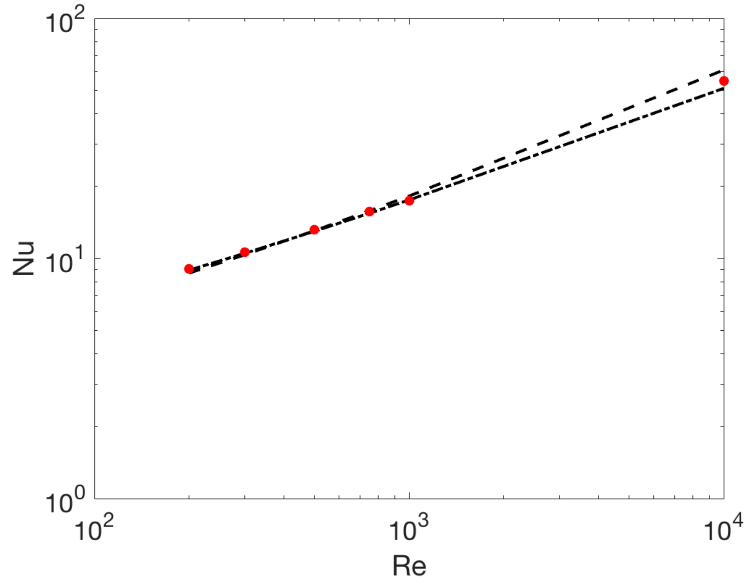

Figure 6: Nusselt number as a function of the Reynolds number. Comparison with the literature:(dashed line) Whitaker [26], (dash-dotted line) Frossling [27]

the experimental measurements, especially those of the heat transfer coefficient. Among these, the support mechanism and its relative position respect the main stream, the turbulence intensity, the scale of turbulence and the heat losses through the support can be found. For instance, Raithby and Eckert [25] analysed some of these aspects and found that placing the stem crossflow results in an increase of the Nusselt number in 10% respect at its position in the rear end of the sphere. Similarly, they detected that 5% increase in the turbulence intensity might represent an increase in the Nusselt number by 7.5% and 17.5% for Reynolds number 3.6×10^3 to 5.2×10^4, respectively.

The local Nusselt number at all Reynolds numbers is shown in figure 7. In figure 7, results of the sphere surface are projected onto a 2D plane; a normal cylindrical projection is used. In the center of this projection, i.e. $[\phi, \psi] \equiv [0, 0]$, the front stagnation point is located, whereas the lines $[\phi, \psi] \equiv [\phi, \pm 90°]$ correspond to single points in the spherical coordinates. In the figure, the white lines indicate the location of the boundary layer separation (see also table 2 where these values are reported). Complementing these contours, plots of the time-average Nusselt number as a function of the angle θ measured from the front stagnation point (figure 8).

At all Reynolds numbers, the attached boundary layer is laminar. Fluctuations in the front zone are rather small up until the flow approaches the line corresponding with the flow separation. In the front stagnation point, the largest value of the Nusselt number is attained (see also figure 8). Then, it decreases monotonically up to a minimum as the laminar boundary layer thickens. This minimum occurs just after the boundary layer separation point (see figure 8 and also the separation location reported in table 2). At $Re = 200$, as the flow is steady and axisymmetric so does the Nusselt number at the surface (see figure 7a). As mentioned before, after the onset of the vortex shedding the wake is asymmetric and this asymmetry also affects the distribution of the heat transfer coefficient in the aft zone of the sphere as can also be noticed in figures 7b-d. As the Reynolds number approaches the chaotic regime $Re \approx 800$ and enters the formation of turbulent vortices in the wake of the sphere, the flow recovers its statistic symmetry and so does the average Nusselt number (see figure 7e,f).

The circumferentially and time averaged Nusselt number is also given in figure 8. In the figure, the Nusselt number is scaled with $Re^{0.5}$ and is compared to data reported in the literature. For Reynolds numbers up to $Re = 750$ (see figure 8a), results are compared to the numerical ones of Bagchi et al. [23] at $Re = 350$ and $Re = 500$ with very good agreement. As the Reynolds increases, the separation point moves towards

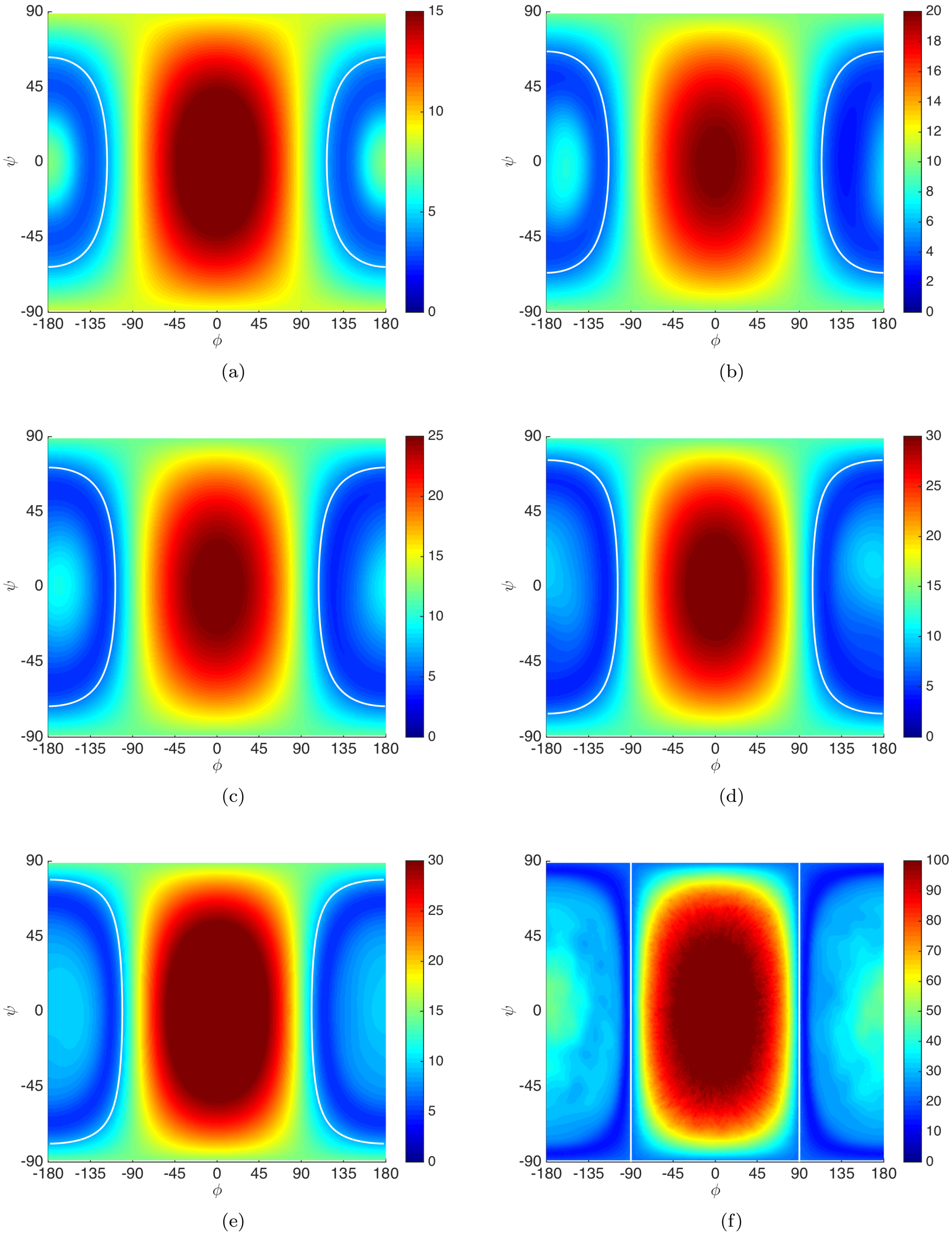

Figure 7: Time average Nusselt number at (a) $Re = 200$, (b) $Re = 300$, (c) $Re = 500$, (d) $Re = 750$, (e) $Re = 1000$ (f) $Re = 10^4$.

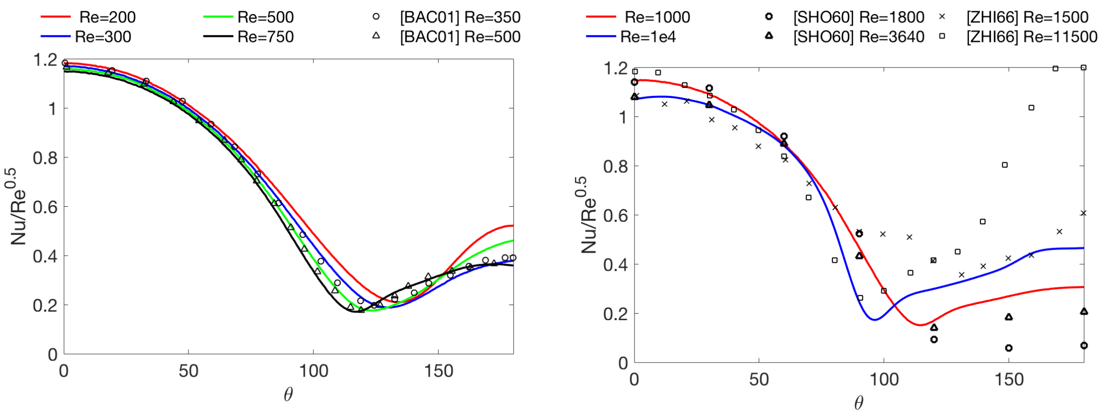

(a)

(b)

Figure 8: Nusselt number variation as a function of the sphere circumference. (a) At low Reynolds numbers, (b) at $Re = 1000$ and $Re = 10^4$, comparison with results from the literature [23, 28, 8].

the sphere apex and the position of the minimum Nusselt number also moves towards lower angular values. However, this local minima is comparable for all Reynolds numbers. For the larger Reynolds numbers, i.e. for Re=1000 and $Re = 10^4$ (see figure 8b), the agreement with the experimental results is fair. Yet, a large scattering is observed probably due to the same issues commented before. As the wake behind the sphere is turbulent, the flow becomes more unstable to disturbances introduced by the support mechanism or the even the incoming turbulence. For these Reynolds numbers, the minimum value is attained at $\theta \approx 114°$ and $\theta \approx 95°$, respectively, after this point the Nusselt number increases moderately towards the rear stagnation point. However, as at $Re = 10^4$ the transition to turbulence is closer to the surface of the sphere than at Re=1000, there is more mixing in the aft region of the sphere and therefore the local values of the Nusselt number are larger in the whole zone.

As commented before, the maximum value of the local Nusselt number is attained at the front stagnation point (see also figure 8); this value does not scale well with $Re^{0.5}$ but slightly decreases as the Reynolds number increases. In figure 9 the Nusselt number at the stagnation point is reported as a function of the Reynolds number. In the figure, correlations from Wadsworth [29] and Sibulkin [30] and the numerical data by Bagchi et al. [23] are also included. The Nusselt number obtained in the present study can be correlated with the Reynolds number as,

$$Re = 1.361\, Re^{0.474} \tag{10}$$

As can be seen from the figure, the agreement of the present data to those reported by Bagchi et al. [23] is quite good. Moreover, although there with some differences the correlation of the present results are also is fair agreement with the correlation proposed by Sibulkin [30] for the range of Reynolds numbers of the present study.

4 Conclusions

High-fidelity numerical simulations of the fluid dynamics and heat transfer of the flow past a sphere at Re numbers of 200, 300, 500, 750, 1000 and 10^4, with $Pr = 0.7$, have been performed in the context of the development of a spherical wind sensor for Mars atmosphere intended for missions after Rover 2020.

After the onset of the vortex shedding (at $Re \approx 210$), the wake behind the sphere is asymmetric for laminar regimes, up to $Re = 800$. This results in non-null lateral forces and non-symmetric heat transfer coefficients. For $Re = 1000$ and 10^4, the shedding occurs at random locations and statistic symmetry is recovered. For $Re = 10^4$, the large scale vortices break into smaller structures forming a turbulent wake.

For all Reynolds numbers, at low angles from the stagnation point the boundary layers have the same

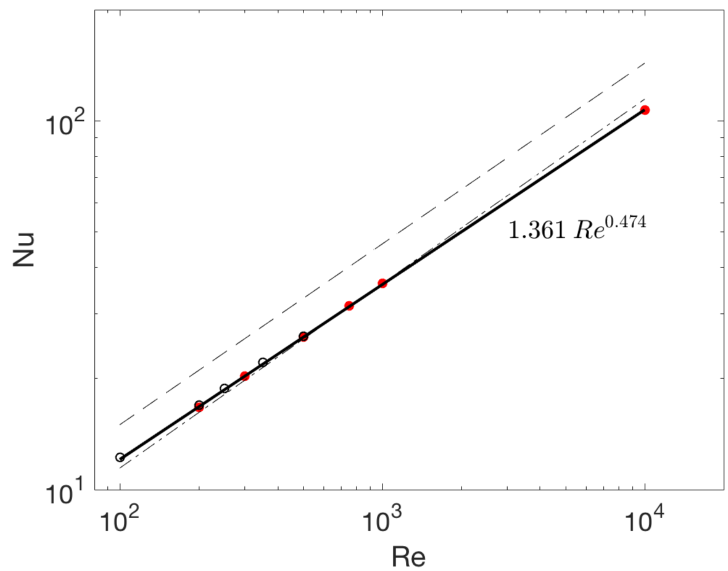

Figure 9: Nusselt number at the front stagnation point. Comparison with correlations reported from the literature (dashed line) Wadswortht ($Nu_{st} = 1.57\ Re^{0.49}$) [29], (dash-dotted line) Sibulkin ($Nu_{st} = 1.144\ Re^{0.5}$)[30] and results from [23] (open circles).

shape factor up until the angle corresponding with the minimum pressure coefficient. The shape factor is slightly lower than the Blasius solution for a laminar boundary layer, with a slight increase in the favorable pressure gradient, followed by a rapid increase in the adverse pressure gradient zone. Separation is reached at $H \approx 3.8 - 4.7$, the larger values correspond with the larger Reynolds numbers. Such behaviour is similar to the subcritical flow around a circular cylinder.

Surface averaged Nusselt numbers obtained are in good agreement with the published experimental results. The discrepancies obtained, especially in local Nusselt numbers at $Re = 1000$ and $Re = 10^4$ are probably due to the sphere supports and the inlet turbulence intensity, that are known to have an important effect and most likely cause scattering of the experimental results. Future numerical simulation works should be aimed to improve the understanding of the effect of turbulent inlet conditions.

As the Reynolds number increases, the separation point and the position of the minimum Nusselt number move towards the sphere apex. At $Re = 10^4$, the transition to turbulence is closer to the surface of the sphere than at $Re = 1000$ and therefore, there is more mixing and larger Nusselt number values in the aft region. The maximum Nusselt number is attained at the front stagnation point; this value can be correlated with Re as $Re = 1.361 Re^{0.474}$, in good agreement with published results.

Acknowledgments

This work has been partially financially supported by the Ministerio de Economía y Competitividad, Secretaría de Estado de Investigación, Desarrollo e Innovación, Spain (refs. ESP2016-79612-C3-2-R & TRA2017-88508-R). We also acknowledge Red Española de Surpercomputación (RES) for awarding us access to the MareNostrum IV machine based in Barcelona, Spain (Ref. FI-2017-2-0012 & FI-2017-3-0018).

References

[1] E. Achenbach. Experiments on the flow past spheres at very high Reynolds numbers. *Journal of Fluid Mechanics*, 54:565–575, 1972.

[2] E. Achenbach. Vortex shedding from spheres. *Journal of Fluid Mechanics*, 62(2):209–221, 1974.

[3] H.J. Kim and P.A. Durbin. Observations of the frequencies in a sphere wake and of drag increase by acoustic excitation. *Physics of Fluids*, 31(11):3260–3265, 1988.

[4] J. S. Wu and G. M. Faeth. Sphere wakes in still surroundings at intermediate Reynolds numbers. *AIAA Journal*, 31(8):1448–1455, 1993.

[5] I. Rodríguez, R. Borrell, O. Lehmkuhl, C. D. Pérez-Segarra, and A. Oliva. Direct numerical simulation of the flow over a sphere at Re = 3700. *Journal of Fluid Mechanics*, 679:263–287, 2011.

[6] I. Rodríguez, O. Lehmkuhl, R. Borrell, and A. Oliva. Flow dynamics in the wake of a sphere at subcritical Reynolds numbers. *Computers & Fluids*, 80:233–243, 2013.

[7] Y. Bazilevs, J. Yan, M. de Stadler, and S. Sarkar. Computation of the Flow Over a Sphere at Re=3700: A Comparison of Uniform and Turbulent Inflow Conditions. *Journal of Applied Mechanics*, 81(12):121003, 2014.

[8] L.K Zhitkevich and L.E. Simchenko. Investigation of local and average heat transfer between a sphere and an airstream. *Journal of Engineering Physics*, 11(1):10–14, 1966.

[9] Gordon L Hayward and David C T Pei. Local heat transfer from a single sphere to a turbulent air stream. *International Journal of Heat and Mass Transfer*, 21:35–41, 1978.

[10] J. B. Will, N. P. Kruyt, and C. H. Venner. An experimental study of forced convective heat transfer from smooth, solid spheres. *International Journal of Heat and Mass Transfer*, 109:1059–1067, 2017.

[11] Lukasz Kowalski, Maria Teresa Atienza, Sergi Gorreta, Vicente Jimenez, Manuel Dominguez-Pumar, Santiago Silvestre, and Luis M. Castañer. Spherical Wind Sensor for the Atmosphere of Mars. *IEEE Sensors Journal*, 16(7):1887–1897, 2016.

[12] A. W. Vreman. The filtering analog of the variational multiscale method in large-eddy simulation. *Physics of Fluids*, 15(8):L61, 2003.

[13] O Lehmkuhl, G Houzeaux, M Avila, H Owen, M Vazquez, and D Mira. A low dissipation finite element scheme for the large eddy simulation on complex geometries. In *19h International Conference on Finite Elements in Flow Problems - FEF 2017*, 2017.

[14] F. Capuano, G. Coppola, L. Rández, and L. de Luca. Explicit Runge-Kutta schemes for incompressible flow with improved energy-conservation properties. *Journal of Computational Physics*, 328:86–94, 2017.

[15] F. X. Trias and O. Lehmkuhl. A self-adaptive strategy for the time integration of Navier-Stokes equations. *Numerical Heat Transfer. Part B*, 60(2):116–134, 2011.

[16] Mariano Vázquez, Guillaume Houzeaux, Seid Koric, Antoni Artigues, Jazmin Aguado-Sierra, Ruth Arís, Daniel Mira, Hadrien Calmet, Fernando Cucchietti, Herbert Owen, Ahmed Taha, Evan Dering Burness, José María Cela, and Mateo Valero. Alya: Multiphysics engineering simulation toward exascale. *Journal of Computational Science*, 14:15–27, 2016.

[17] A. Tomboulides and S.A. Orszag. Numerical investigation of transitional and weak turbulent flow past a sphere. *Journal of Fluids Mechanics*, 416:45–73, 2000.

[18] H. Sakamoto and H. Haniu. A study on vortex sheding from spheres in an uniform flow. *Journal of Fluids Engineering*, 112:386–392, 1990.

[19] G. Constantinescu, M. Chapelet, and K. Squires. Turbulence modeling applied to flow over a sphere. *AIAA Journal*, 41(9):1733–1741, 2003.

[20] G. Yun, D. Kim, and H. Choi. Vortical structures behind a sphere at subcritical Reynolds numbers. *Physics of Fluids*, 18, 2006.

[21] T. A. Johnson and V. C. Patel. Flow past a sphere up to a Reynolds number of 300. *Journal of Fluid Mechanics*, 378:19–70, January 1999.

[22] J. Jeong and Hussain Fazle. On the identification of a vortex. *Journal of Fluids Mechanics*, 285(69–94), 1995.

[23] P. Bagchi, M.Y. Ha, and S. Balachandar. Direct numerical simulation of flow and heat transfer from a sphere in a uniform cross-flow. *Journal of Fluids Engineering*, 123:347–358, 2001.

[24] W. Cheng, D. I. Pullin, R. Samtaney, W. Zhang, and W. Gao. Large-eddy simulation of flow over a cylinder with from to : a skin-friction perspective. *Journal of Fluid Mechanics*, 820:121–158, 2017.

[25] G D Raithby and E R G Eckert. The effect of turbulence parameters and support position on the heat transfer from spheres. *International Journal of Heat and Mass Transfer*, 11:1233–1252, 1968.

[26] Stephen Whitaker. Forced Convection Heat Transfer Correlations for Flow In Pipes, Past Flat Plates, Single cylinders, single spheres, and flow in packed beds and tube bundles. *AIChE Journal*, 18(2):361–

371, 1972.

[27] N. Frössling. Evaporation, heat transfer, and velocity distribution in two-dimensional and rotationally symmetrical laminar boundary layer flow. Technical report, 1956.

[28] W. W. Short, R. A. S. Brown, and B. H. Sage. Thermal Transfer in Turbulent Gas Streams. Effect of Turbulence on Local Transport From Spheres. *Journal of Applied Mechanics*, 27(3):393–402, 1960.

[29] J. Wadsworth. The experimental examination of the local heat transfer on the surface of a sphere when subjected to forced convective cooling. Technical report, National Research Counsil, Canada Division. MT-39, 1958.

[30] M Sibulkin. Heat transfer near the forward stagnation point of a body of revolution. *Journal of Aeronautical Sciences*, 19(8):570, 1952.